Simultaneous Femtosecond X-ray Spectroscopy and Diffraction of Photosystem II at Room Temperature

Jan Kern *et al.*

Science **340**, 491 (2013);
DOI: 10.1126/science.1234273

Science (print ISSN 0036-8075; online ISSN 1095-9203) is published weekly, except the last week in December, by the American Association for the Advancement of Science, 1200 New York Avenue NW, Washington, DC 20005.

the observed relationships between recruitment/survival and mismatch (*21*), and projected the population forward in time under the same three scenarios of climate change as described in (*27*). For each scenario, predicted changes in *PM* were first calculated using output from models of great tit and caterpillar phenology described in (*27*) and then used as inputs to the current simulation model. The simulations showed that a gradual decline in population size would result if *PM* increases over the next century (assuming no evolutionary response and the same DDC in recruitment rates as observed in the historical data), with the decline being strongest under the most extreme scenario of climate change (Fig. 3A). When DDC in recruitment rates was 'turned off' in the simulations, the rate of population decline for each scenario became substantially stronger (Fig. 3B). This demonstrates that DDC modulates the impacts of mismatch on population growth by partially buffering the population from otherwise more rapid declines.

We found that increasing phenological mismatch driven by climate change had little effect on population growth rates over a study period of almost four decades, despite intensifying directional selection on laying dates. Population numbers therefore remained stable even though late spring temperatures increased by 3.7°C (*21*). Density dependence within the life cycle partially buffered population growth rate against the negative effects of environmental change, in effect dampening the demographic cost of directional selection. Indeed, theory suggests that the magnitude of the lag load will depend on the form and strength of density regulation, as well as the magnitude of stochastic environmental fluctuations (*28*). The DDC mechanism we describe here is therefore likely to be of general importance in a wide range of species. For example, Wilson and Arcese (*29*) found that the population growth of song sparrows was not affected by year-to-year variation in the timing of breeding, despite the latter being strongly correlated with climate. They suggested, but did not demonstrate explicitly, that DDC in recruitment rates could explain this uncoupling. Similar buffering mechanisms might also play a role in dampening the effects of climate change on density-regulated mammal populations, although reductions in mean fitness may be unavoidable when large phenological changes occur (*30*). Further studies characterizing the lag load in wild populations with different life histories will be crucial to understanding and predicting climate change impacts on population dynamics. Evolutionary adaptation will be critical for persistence in the long run (*27*), but our results imply that considerable directional selection might be demographically tolerable on decadal time scales without immediate population declines, effectively buying time for microevolution to restore adaptation.

References and Notes

1. J. G. Kingsolver, D. W. Pfennig, *Bioscience* **57**, 561 (2007).
2. D. S. Falconer, T. F. C. Mackay, *Introduction to Quantitative Genetics* (Longmans Green, Harlow, Essex, UK, ed. 4, 1996).
3. M. E. Visser, *Proc. Biol. Sci.* **275**, 649 (2008).
4. L. M. Chevin, R. Lande, G. M. Mace, *PLoS Biol.* **8**, e1000357 (2010).
5. M. Lynch, R. Lande, in *Biotic Interactions and Global Change*, P. M. Kareiva, J. G. Kingsolver, R. B. Huey, Eds. (Sinauer, Sunderland, MA, 1993), pp. 234–250.
6. R. Bürger, M. Lynch, *Evolution* **49**, 151 (1995).
7. J. J. Hellmann, M. Pineda-Krch, *Biol. Conserv.* **137**, 599 (2007).
8. R. Lande, *Evolution* **61**, 1835 (2007).
9. R. Lande, S. Shannon, *Evolution* **50**, 434 (1996).
10. R. Gomulkiewicz, R. D. Holt, *Evolution* **49**, 201 (1995).
11. M. T. Kinnison, N. G. Hairston, *Funct. Ecol.* **21**, 444 (2007).
12. R. Bürger, C. Krall, in *Evolutionary Conservation Biology*, R. Ferriere, U. Dieckmann, D. Couvet, Eds. (Cambridge Univ. Press, Cambridge, 2004), pp. 171–187.
13. N. G. Hairston Jr., S. P. Ellner, M. A. Geber, T. Yoshida, J. A. Fox, *Ecol. Lett.* **8**, 1114 (2005).
14. M. E. Visser, C. Both, *Proc. Biol. Sci.* **272**, 2561 (2005).
15. A. J. Miller-Rushing, T. T. Hoye, D. W. Inouye, E. Post, *Philos. Trans. R. Soc. London Ser. B* **365**, 3177 (2010).
16. M. E. Visser, A. J. van Noordwijk, J. M. Tinbergen, C. M. Lessells, *Proc. R. Soc. London B Biol. Sci.* **265**, 1867 (1998).
17. M. E. Visser, L. J. M. Holleman, P. Gienapp, *Oecologia* **147**, 164 (2006).
18. A. Charmantier *et al.*, *Science* **320**, 800 (2008).
19. A. J. van Noordwijk, R. H. McCleery, C. M. Perrins, *J. Anim. Ecol.* **64**, 451 (1995).
20. V. Grøtan *et al.*, *J. Anim. Ecol.* **78**, 447 (2009).
21. Materials and methods are available as supplementary materials on *Science* Online.
22. D. W. Thomas, J. Blondel, P. Perret, M. M. Lambrechts, J. R. Speakman, *Science* **291**, 2598 (2001).
23. T. E. Reed, S. Jenouvrier, M. E. Visser, *J. Anim. Ecol.* **82**, 131 (2013).
24. C. Both, M. E. Visser, N. Verboven, *Proc. R. Soc. London B Biol. Sci.* **266**, 465 (1999).
25. M. S. Boyce, A. Sinclair, G. C. White, *Oikos* **87**, 419 (1999).
26. K. A. Rose, J. H. Cowan, K. O. Winemiller, R. A. Myers, R. Hilborn, *Fish Fish.* **2**, 293 (2001).
27. P. Gienapp *et al.*, *Philos. Trans. R. Soc. London Ser. B* **368**, 20120289 (2013).
28. R. Lande, S. Engen, B. E. Saether, *Philos. Trans. R. Soc. London Ser. B* **364**, 1511 (2009).
29. S. Wilson, P. Arcese, *Proc. Natl. Acad. Sci. U.S.A.* **100**, 11139 (2003).
30. J. E. Lane, L. E. B. Kruuk, A. Charmantier, J. O. Murie, F. S. Dobson, *Nature* **489**, 554 (2012).
31. A. Gosler, *The Great Tit* (Hamlyn, London, 1993).
32. V. Bauchau, A. Van Noordwijk, *J. Appl. Stat.* **22**, 1031 (1995).
33. H. Schielzeth, *Methods Ecol. Evol.* **1**, 103 (2010).

Acknowledgments: Stichting Nationaal Park De Hoge Veluwe kindly gave permission to work in their woodlands. The authors thank the many fieldworkers who have contributed to data collection over the years. M. Kinnison, R. Waples, K. Lessells, and P. Gienapp provided valuable comments. M.E.V. is supported by a Netherlands Organisation for Scientific Research–VICI grant. M.E.V. supervised the long-term population study; T.E.R., M.E.V., B.-E.S., V.G., and S.J. conceived the questions and analyses; T.E.R. and V.G. analyzed the data; and T.E.R. and M.E.V. wrote the paper. Data, results, and the R code for the simulation model are available on Dryad (http://datadryad.org).

Supplementary Materials

www.sciencemag.org/cgi/content/full/340/6131/488/DC1
Materials and Methods
Figs. S1 and S2
References (*31*–*33*)

16 November 2012; accepted 21 February 2013
10.1126/science.1232870

Simultaneous Femtosecond X-ray Spectroscopy and Diffraction of Photosystem II at Room Temperature

Jan Kern,[1,2] Roberto Alonso-Mori,[2] Rosalie Tran,[1] Johan Hattne,[1] Richard J. Gildea,[1] Nathaniel Echols,[1] Carina Glöckner,[3] Julia Hellmich,[3] Hartawan Laksmono,[4] Raymond G. Sierra,[4] Benedikt Lassalle-Kaiser,[1]* Sergey Koroidov,[5] Alyssa Lampe,[1] Guangye Han,[1] Sheraz Gul,[1] Dörte DiFiore,[3] Despina Milathianaki,[2] Alan R. Fry,[2] Alan Miahnahri,[2] Donald W. Schafer,[2] Marc Messerschmidt,[2] M. Marvin Seibert,[2] Jason E. Koglin,[2] Dimosthenis Sokaras,[6] Tsu-Chien Weng,[6] Jonas Sellberg,[6,7] Matthew J. Latimer,[6] Ralf W. Grosse-Kunstleve,[1] Petrus H. Zwart,[1] William E. White,[2] Pieter Glatzel,[8] Paul D. Adams,[1] Michael J. Bogan,[2,4] Garth J. Williams,[2] Sébastien Boutet,[2] Johannes Messinger,[5] Athina Zouni,[3] Nicholas K. Sauter,[1] Vittal K. Yachandra,[1]† Uwe Bergmann,[2]† Junko Yano[1]†

Intense femtosecond x-ray pulses produced at the Linac Coherent Light Source (LCLS) were used for simultaneous x-ray diffraction (XRD) and x-ray emission spectroscopy (XES) of microcrystals of photosystem II (PS II) at room temperature. This method probes the overall protein structure and the electronic structure of the Mn_4CaO_5 cluster in the oxygen-evolving complex of PS II. XRD data are presented from both the dark state (S_1) and the first illuminated state (S_2) of PS II. Our simultaneous XRD-XES study shows that the PS II crystals are intact during our measurements at the LCLS, not only with respect to the structure of PS II, but also with regard to the electronic structure of the highly radiation-sensitive Mn_4CaO_5 cluster, opening new directions for future dynamics studies.

One of the metalloenzymes most critical for sustaining aerobic life is photosystem II (PS II)—a membrane-bound protein complex found in green plants, algae, and cyanobacteria—that catalyzes the light-driven water oxidation reaction. The oxidation equivalents

generated by the absorption of four photons by the PS II reaction center are stored in the four consecutive redox states of a Mn_4CaO_5 cluster, known as the S_i (i = 1 to 4) states. The accumulated energy is used in the concerted oxidation of two molecules of water to form dioxygen (*1*), returning the catalyst to the most reduced S_0 state in the Kok cycle (Scheme 1). Due to its efficient catalysis of the demanding four-electron and four-proton chemistry of water oxidation, the Mn_4CaO_5 cluster has been a model system for synthesizing inorganic water oxidation catalysts (*2*, *3*).

The structure of PS II in its dark stable state (S_1) was studied extensively using x-ray diffraction (XRD) measurements on cryo-cooled crystals (*4*–*7*) at synchrotron radiation (SR) sources with resolutions ranging from 3.8 to 1.9 Å. One inherent limitation of XRD measurements on this system, however, is the high radiation sensitivity of the Mn_4CaO_5 cluster. An increase of the average metal-ligand and metal-metal distances is observed in the XRD data as compared with the extended x-ray absorption fine structure (EXAFS) data that were collected below the threshold of radiation damage [reviewed in (*8*)], indicating that the structure of the cluster is either altered or disrupted. Such specific damage (photoreduction of the metal center) (*9*, *10*) occurred despite the fact that all XRD measurements were carried out at cryogenic temperatures of 100 to 150 K. It is now generally recognized that for some other redox-active metalloproteins, it is difficult to obtain intact structures with SR-based XRD, even at cryogenic temperatures (*11*, *12*). Recently, a new approach to protein crystallography was demonstrated at the X-ray Free-Electron Laser (XFEL) of the Linac Coherent Light Source (LCLS), with ultrashort x-ray pulses of high intensity enabling collection of diffraction data at room temperature (RT) before the onset of radiation damage in various systems (*13*–*18*).

Whereas XRD is powerful in determining the overall protein structure, various x-ray spectroscopy techniques can provide critical complementary information about the active site due to their element and chemical sensitivity (*8*, *19*–*22*). To understand the intricate interplay between protein and metal cofactors that allows complex reactions, it is desirable to combine both approaches in time-resolved studies under functional conditions.

Among the various spectroscopic methods, nonresonant x-ray emission spectroscopy (XES) probes occupied electron levels (see Fig. 1, bottom right). In particular, the $K\beta_{1,3}$ line is a probe of the number of unpaired 3d electrons, hence providing information about the oxidation and/or spin state (*22*). Experimentally, XES performed using an energy-dispersive x-ray spectrometer (*23*) is particularly well suited for such combined shot-by-shot studies, as excitation energies above the 1s core hole of first-row transition metals are also ideal for XRD; therefore, neither incident nor emitted photon energy need to be scanned. Although it has been demonstrated that the shot-by-shot approach can probe the atomic structure of intact proteins at high resolution (*17*), the question has remained whether ultrabright femtosecond pulses can also probe the intact electronic structure of active centers such as the Mn_4CaO_5 cluster. This is by no means obvious, because, in contrast to XRD, in which radiation-induced damage leads to loss of diffractivity, such a self-termination of the signal is not expected in XES, and electronic structural changes happen on a much faster time scale than a Coulomb explosion. Recently, we used solutions of Mn model systems (*24*) in a liquid jet (*25*) at LCLS to demonstrate the feasibility of RT femtosecond Kβ XES.

Building on the feasibility of these separate femtosecond XRD studies of PS II (*18*) and femtosecond XES results, we have designed an experimental setup for simultaneous XRD and XES data collection at the LCLS. We used XES to determine the electronic-state integrity of the Mn_4CaO_5 cluster. Simultaneously, we used a visible-laser pump (centered at 527 nm) and an x-ray laser probe to collect RT XRD measurements of the S_2 state, and we compared our results with the XRD data from the dark S_1 state. The schematic of the setup is shown in Fig. 1 (*26*). Suspensions of PS II microcrystals (5 to 15 μm in the longest dimension) were

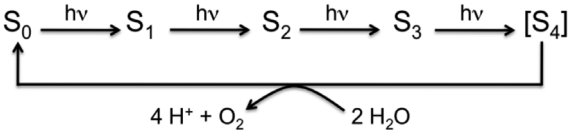

Scheme 1. Reaction cycle of water oxidation at the Mn_4CaO_5 cluster in PS II. h, Planck's constant; ν, frequency.

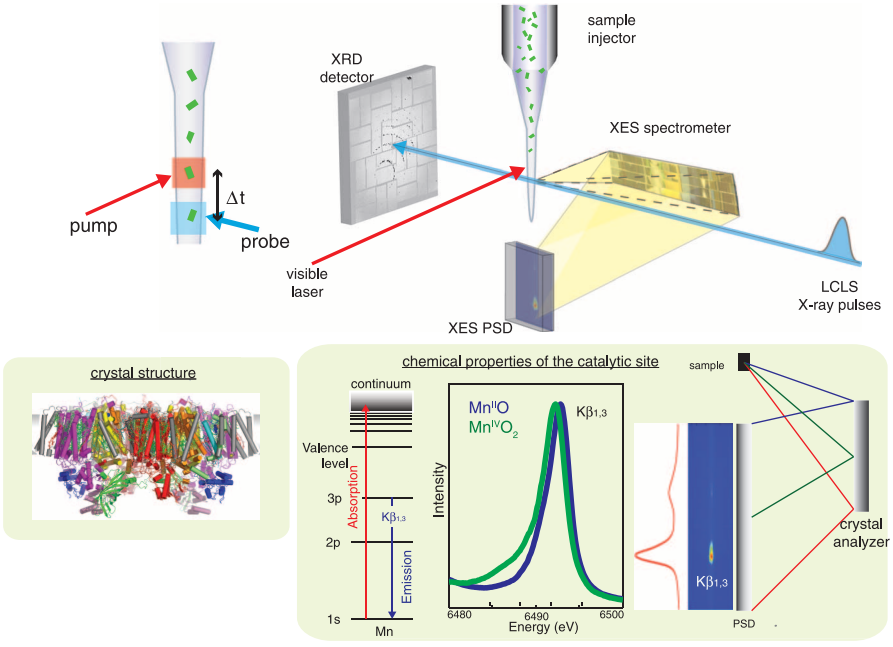

Fig. 1. Setup of simultaneous x-ray spectroscopy and crystallography experiment at the CXI instrument of LCLS. The crystal suspension is electric-field–focused into a microjet that intersects the x-ray pulses. XRD data from a single crystal are collected downstream with a CSPAD detector, and XES data from the same crystal are collected at ~90° to the beam via a multicrystal XES spectrometer and a compact position-sensitive detector (PSD). A Nd-YLF laser (527 nm) is used to illuminate the crystals. The timing protocol (top left) consists of a fixed time of flight Δt between the optical pump and x-ray probe. The schematic of the energy dispersive spectrometer is shown (bottom right), as well as the Mn^{II} and Mn^{IV} oxide $K\beta_{1,3}$ spectra and an energy-level diagram for XES (bottom middle).

[1]Physical Biosciences Division, Lawrence Berkeley National Laboratory, Berkeley, CA 94720, USA. [2]Linac Coherent Light Source (LCLS), SLAC National Accelerator Laboratory, Menlo Park, CA 94025, USA. [3]Max-Volmer-Laboratorium für Biophysikalische Chemie, Technische Universität, D-10623 Berlin, Germany. [4]PULSE Institute, SLAC National Accelerator Laboratory, Menlo Park, CA 94025, USA. [5]Institutionen för Kemi, Kemiskt Biologiskt Centrum, Umeå Universitet, Umeå, Sweden. [6]Stanford Synchrotron Radiation Lightsource (SSRL), SLAC National Accelerator Laboratory, Menlo Park, CA 94025, USA. [7]Department of Physics, AlbaNova, Stockholm University, S-106 91 Stockholm, Sweden. [8]European Synchrotron Radiation Facility, F-38043 Grenoble Cedex 9, France.

*Present address: Synchrotron SOLEIL, F-91192 Gif-Sur-Yvette, France.

†Corresponding author. E-mail: vkyachandra@lbl.gov (V.K.Y.); bergmann@slac.stanford.edu (U.B.); jyano@lbl.gov (J.Y.)

injected into the coherent x-ray imaging (CXI) chamber (*27*) at LCLS using an electrospun liquid microjet (*25*) to intersect the x-ray pulses (~50-fs pulse length, peak x-ray dose of ~150 megagray per pulse). We used a Cornell-SLAC pixel array detector (CSPAD) (*28*) to collect XRD data. Mn $K\beta_{1,3}$ XES data were collected simultaneously from the same sample using an energy-dispersive spectrometer at ~90° to the beam direction and a small CSPAD (*26*).

The dark-adapted PS II microcrystals showed diffraction spots to 4.1 Å in the best cases (fig. S1). Within 5 hours of run time (corresponding to nearly 2,200,000 x-ray shots), we collected 90,000 shots identified as potential hits (16 or more strong Bragg peaks). Out of these, 4663 shots were indexed and integrated (tables S1 and S2). We processed the diffraction data to a resolution of 5.7 Å to generate the electron density map shown in Fig. 2, A and B [the 5.7 Å cutoff was chosen on the basis of the multiplicity and completeness (tables S1 and S2)]. However, we indexed Bragg spots to 4.1 Å resolution, and the signal strength, as measured by $I/\sigma(I)$ (the ratio of the spot's peak intensity to its standard deviation), was still 1.9 out to 5 Å resolution (table S2).

The improved resolution of the electron density compared with that reported earlier at 6.5 Å resolution (*18*) is manifested in a more detailed map allowing for better tracing of the transmembrane helices and of the loop regions in the membrane extrinsic areas of the complex facing the inner compartment of the thylakoid (lumen) and the cytoplasm (stroma). There is good agreement between the 5.7 Å resolution electron density from the XFEL data (Fig. 2A) and previously collected (*6*) SR data [Protein Data Bank identification number (PDB ID) 3bz1] truncated at 5.7 Å. Despite slight nonisomorphism between the XFEL and SR data sets, the maps have an overall correlation coefficient (CC) of 0.36 (a CC of 0 means no correlation; a CC of 1 indicates full correlation).

The influence of the phasing model on the electron density omit maps was tested by excluding heavy elements (see supplementary materials and fig. S2). The use of random or uniform structure factors instead of the experimental data did not generate any density peaks in the omit maps in the region of the Mn_4CaO_5 cluster, confirming that the density observed is from the experimental data (fig. S3). It is similar to the density obtained from the SR data but is slightly more compact (Fig. 2B).

Figure 3A shows the $K\beta_{1,3}$ x-ray emission spectra from PS II crystals collected simultaneously with the XRD data. The spectra average ~20,000 shots, recorded at 7-keV incident energy, that we identified as crystal hits from the XRD data. To illustrate the sensitivity of this measurement, we estimated that the volume of sample probed by x-rays for this spectrum is ~0.3 nl, containing a total of 2×10^{-12} mol Mn. A spectrum using only data from crystals that yield indexable diffraction patterns was computed as well (fig. S4). Both spectra coincide in peak position and shape and differ only in the signal-to-noise (S/N) ratio due to the different number of samples used for each of them. The spectrum of PS II crystals matches very well with the spectrum from dark-adapted PS II solution (S_1 state) (8.9 mM Chl, 1 mM Mn, 375,000 individual shots) collected with the same setup at the CXI instrument (Fig. 3B). This implies that the Mn cluster is in the same high-valent state ($Mn_2^{III}Mn_2^{IV}$) in both micrometer-sized crystals and solution and that the crystallization procedure did not alter the native PS II S_1 state.

We used the SR solution data collected at 8 K and at RT to compare the shape and energy position of the spectra. The RT SR spectrum represents a completely photoreduced (damaged) PS II (Fig. 3C, pink), where all Mn is reduced to Mn^{II} and the $K\beta_{1,3}$ peak is shifted toward the position found for $Mn^{II}Cl_2$ in aqueous solution (Fig. 3C, gray). The 8-K SR spectrum is from an intact PS II S_1 state (Fig. 3C, light blue). It is evident that the XFEL PS II XES data at RT are identical to the intact S_1 state spectrum. Note that we used roughly the same x-ray dose for the XFEL and the SR measurements at RT (total number of photons per sample spot for the SR data and the number of photons per shot for the XFEL data). The result clearly demonstrates

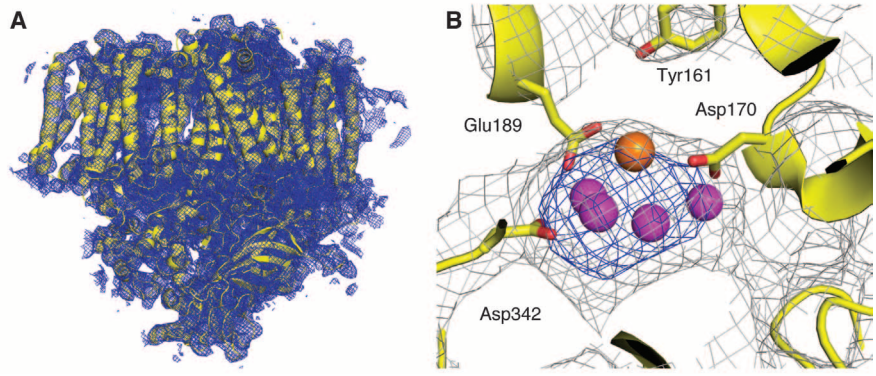

Fig. 2. Structure deduced from diffraction of micrometer-sized crystals of PS II using sub–50-fs x-ray pulses at RT at LCLS. (**A**) $2mF_o$-DF_c electron density map for the PS II complex in the dark S_1 state obtained at LCLS. One monomer of the protein is shown in yellow, and the electron density is contoured at 1.2σ (blue mesh; shown for a radius of 5 Å around the protein). (**B**) Detail of the same map in the area of the Mn_4CaO_5 cluster in the dark S_1 state, with mesh contoured at 1.0σ (gray) and 4.0σ (blue). Selected residues from subunit D1 are labeled for orientation; Mn is shown as purple spheres and Ca as an orange sphere (metal positions taken from PDB ID 3bz1).

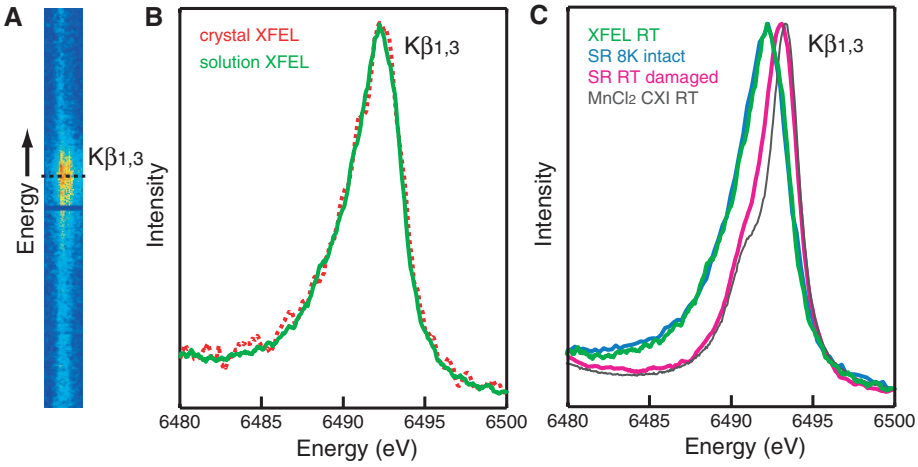

Fig. 3. Femtosecond XES of PS II. (**A**) Two-dimensional (2D) $K\beta_{1,3}$ x-ray emission spectra from microcrystals of PS II collected with a PSD at the CXI instrument using sub–50-fs pulses of about 2 to 3×10^{11} photons per μm^2 and pulse. (**B**) X-ray emission spectra of a solution of PS II (green curve) and single crystals of PS II (red dashed curve) in the dark state, both collected at the CXI instrument, obtained from the 2D plot in (A) by integration along the horizontal axis. (**C**) X-ray emission spectra of PS II solutions in the dark state collected at the CXI instrument at RT (green) or collected using SR under cryogenic conditions with a low x-ray dose ("8K intact," light blue) or SR at RT under photoreducing conditions ("RT damaged," pink). The spectrum from $Mn^{II}Cl_2$ in aqueous solution collected at RT at the CXI instrument is shown (gray) for comparison.

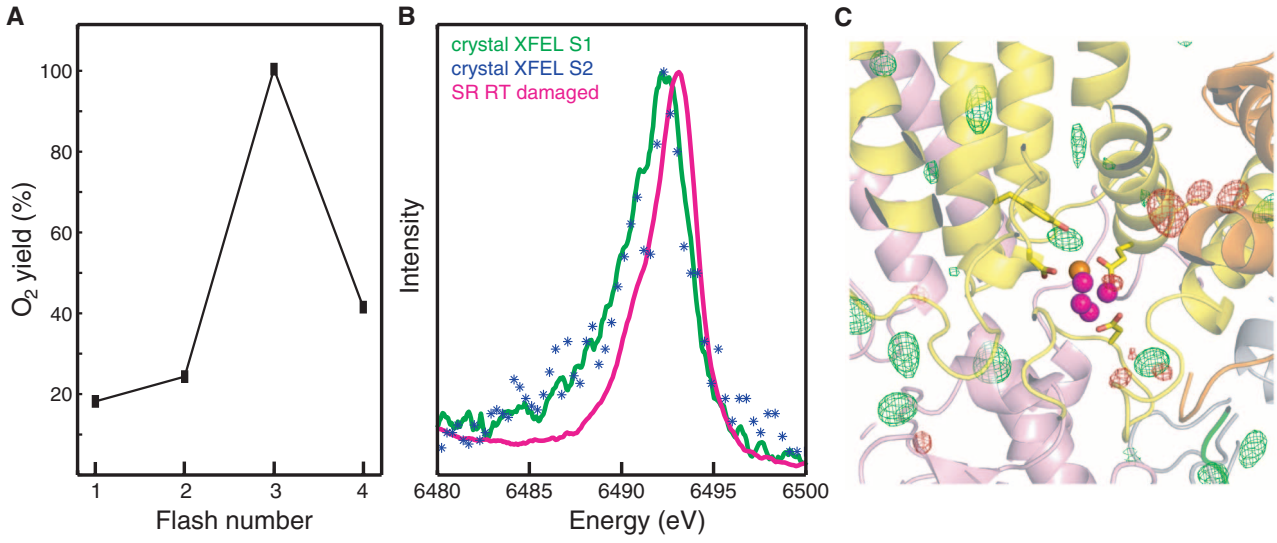

Fig. 4. Characterization of the illuminated PS II sample. (**A**) On-line MIMS measurements of light-induced O_2 yield detected as mixed labeled $^{16}O^{18}O$ species after illumination of photosystem II from *Thermosynechococcus elongatus*. The data shows that >73% of the sample occupies the S_2 state after one illumination. (**B**) XFEL XES of PS II in the S_2 state. The $K\beta_{1,3}$ XES data collected from 362 microcrystals of PS II in the first illuminated S_2 state are shown in blue (asterisks). The XFEL spectrum of microcrystals of PS II in the dark stable S_1 state is shown in green. For comparison, an x-ray emission spectrum of completely photoreduced ("damaged") PS II collected at RT at a synchrotron is shown in pink. (**C**) Isomorphous difference map between the XFEL-illuminated (S_2 state) and XFEL-dark (S_1 state) XRD data set in the region of the Mn_4CaO_5 cluster, with F_o-F_o difference contours shown at +3σ (green mesh) and −3σ (red mesh); histogram analysis indicates that this map is statistically featureless (fig. S6). Metal ions of the Mn_4CaO_5 cluster are shown for orientation as purple (Mn) and orange (Ca) spheres; subunits are indicated in yellow (D1), orange (D2), pink (CP43), and green (PsbO).

that the femtosecond x-ray pulses, under the conditions presented here, can be used to obtain the intact x-ray emission spectrum of the highly reduction-sensitive, damage-prone Mn_4CaO_5 cluster of PS II at RT. The XES data prove that the XRD data and the electron density are from PS II with a fully intact Mn_4CaO_5 cluster in the S_1 state ($Mn_2^{III}Mn_2^{IV}$) under the conditions of the current experiment.

The confirmation of an intact Mn_4CaO_5 cluster in PS II at RT allowed us to explore the illuminated state (S_2 state) with a visible-laser pump followed by an x-ray laser probe pulse. The crystals were illuminated in situ using the 527-nm output of a Nd–yttrium-lithium-fluoride (Nd-YLF) laser with a delay time between optical and x-ray exposure of 0.4 to 0.5 s (*26*). Advancement of the PS II sample into the S_2 state was tested independently with a similar illumination setup coupled to a membrane inlet mass spectrometer (MIMS) using water labeled with oxygen-18. Analysis of the labeled O_2 produced as a function of the number of laser flashes showed that an S_2 state population of ~80% was achieved with one flash (Fig. 4A and supplementary materials).

Using the same illumination conditions for PS II microcrystals at the CXI instrument, we obtained ~4300 indexed diffraction patterns within a collection time of 53 min (corresponding to ~380,000 shots). Out of these, 1850 diffraction images were included in the data set (XFEL-illuminated) with a final resolution of 5.9 Å. The statistics for both XFEL-dark and XFEL-illuminated data sets are given in tables S1 to S3. In parallel with the XRD, we also collected XES data for these crystals. The resulting spectrum from 362 illuminated microcrystals recorded with an incident energy of 7 keV is shown in Fig. 4B (XFEL S_2). Despite the lower S/N ratio of the S_2 state spectrum, because of the fewer number of crystals sampled (a factor of ~50), the spectrum matches well with the x-ray emission spectrum obtained for crystals in the S_1 state. Detection of the expected shift (~60 meV) in the x-ray emission spectrum between the S_1 and S_2 states (*20*) requires a much better S/N ratio. However, it is evident that the XFEL S_2 state spectrum is different from the damaged spectrum, which clearly demonstrates that the Mn_4CaO_5 cluster is not photoreduced by our optical illumination pump protocol or the x-ray pulse.

The RT electron density maps of the dark and illuminated states are similar within the error of the resolution, with an overall CC of 0.77. An isomorphous difference map computed between the dark and illuminated data set showed no statistically significant peaks (Fig. 4C and figs. S5 and S6), and closer inspection of the region of the Mn_4CaO_5 cluster (Fig. 4C) and the stromal electron-acceptor side of the complex (fig. S5B) did not reveal any interpretable features in these regions. This shows that our illumination conditions do not lead to decay or changes in the crystal quality. More importantly, this finding suggests that there are no large structural changes taking place between the S_1 and S_2 states. Although the S_1-S_2 transition is accompanied by a number of changes in carboxylate and backbone vibration frequencies, as detected by infrared spectroscopy (*29*, *30*), the associated structural changes are most likely too small to be detected by the resolution achieved in the present study.

In summary, we have established that simultaneous XRD and XES studies using ultrashort, ultrabright x-ray pulses at LCLS can probe the intact atomic structure of PS II microcrystals and the intact electronic structure of its Mn_4CaO_5 cluster at RT. This technique can be used for future time-resolved studies of light-driven structural changes within proteins and cofactors and of chemical dynamics at the catalytic metal center under functional conditions. We expect that this method will be applicable to many metalloenzymes, including those that are known to be very sensitive to x-ray photoreduction and radiation damage, and over a wide range of time scales, starting with femtoseconds.

References and Notes

1. G. Renger, in *Photosynthesis: Plastid Biology, Energy Conversion and Carbon Assimilation*, J. J. Eaton-Rye, B. C. Tripathy, T. D. Sharkey, Eds. (Springer, Dordrecht, Netherlands, 2012), pp. 359–414.
2. J. S. Kanady, E. Y. Tsui, M. W. Day, T. Agapie, *Science* **333**, 733 (2011).
3. S. Mukherjee *et al.*, *Proc. Natl. Acad. Sci. U.S.A.* **109**, 2257 (2012).
4. A. Zouni *et al.*, *Nature* **409**, 739 (2001).
5. K. N. Ferreira, T. M. Iverson, K. Maghlaoui, J. Barber, S. Iwata, *Science* **303**, 1831 (2004).
6. A. Guskov *et al.*, *Nat. Struct. Mol. Biol.* **16**, 334 (2009).
7. Y. Umena, K. Kawakami, J. R. Shen, N. Kamiya, *Nature* **473**, 55 (2011).
8. J. Yano, V. K. Yachandra, *Inorg. Chem.* **47**, 1711 (2008).
9. J. Yano *et al.*, *Proc. Natl. Acad. Sci. U.S.A.* **102**, 12047 (2005).

10. M. Grabolle, M. Haumann, C. Müller, P. Liebisch, H. Dau, *J. Biol. Chem.* **281**, 4580 (2006).
11. M. C. Corbett *et al.*, *Acta Crystallogr.* **D63**, 951 (2007).
12. Y. T. Meharenna, T. Doukov, H. Li, S. M. Soltis, T. L. Poulos, *Biochemistry* **49**, 2984 (2010).
13. H. N. Chapman *et al.*, *Nature* **470**, 73 (2011).
14. R. A. Kirian *et al.*, *Acta Crystallogr.* **A67**, 131 (2011).
15. M. S. Hunter *et al.*, *Biophys. J.* **100**, 198 (2011).
16. A. Barty *et al.*, *Nat. Photonics* **6**, 35 (2012).
17. S. Boutet *et al.*, *Science* **337**, 362 (2012).
18. J. Kern *et al.*, *Proc. Natl. Acad. Sci. U.S.A.* **109**, 9721 (2012).
19. J. Yano *et al.*, *Science* **314**, 821 (2006).
20. J. Messinger *et al.*, *J. Am. Chem. Soc.* **123**, 7804 (2001).
21. Y. Pushkar *et al.*, *Angew. Chem. Int. Ed.* **49**, 800 (2010).
22. P. Glatzel, U. Bergmann, *Coord. Chem. Rev.* **249**, 65 (2005).
23. R. Alonso-Mori *et al.*, *Rev. Sci. Instrum.* **83**, 073114 (2012).
24. R. Alonso-Mori *et al.*, *Proc. Natl. Acad. Sci. U.S.A.* **109**, 19103 (2012).
25. R. G. Sierra *et al.*, *Acta Crystallogr. D Biol. Crystallogr.* **68**, 1584 (2012).
26. Materials and methods are available as supplementary materials on *Science* Online.
27. S. Boutet, G. J. Williams, *New J. Phys.* **12**, 035024 (2010).
28. P. Hart *et al.*, *Proc. SPIE* **8504**, 85040C (2012).
29. R. J. Debus, *Coord. Chem. Rev.* **252**, 244 (2008).
30. M. Iizasa, H. Suzuki, T. Noguchi, *Biochemistry* **49**, 3074 (2010).

Acknowledgments: We dedicate this paper to G. Renger (1937–2013) for his enthusiasm and support. This work was supported by the Director, Office of Science, Office of Basic Energy Sciences (OBES), Division of Chemical Sciences, Geosciences, and Biosciences (CSGB) of the Department of Energy (DOE) under contract DE-AC02-05CH11231 (J.Y. and V.K.Y.) for x-ray methodology and instrumentation; a Laboratory Directed Research and Development award to N.K.S; NIH grant GM055302 (V.K.Y.) for PS II biochemistry, structure, and mechanism and NIH grant P41GM103393 (U.B.); and grants GM095887 and GM102520 (N.K.S.) for data-processing methods. We thank the Deutsche Forschungsgemeinschaft Cluster of Excellence "UniCat," coordinated by the Technische Universität Berlin and Sfb1078, TP A5 (A.Z.); the Alexander von Humboldt Foundation (J.K.); and the Solar Fuels Strong Research Environment (Umeål University), the Artificial Leaf Project (K&A Wallenberg Foundation), and Vetenskapsrådet and Energimyndigheten (J.M.) for supporting this project. The injector work was supported by LCLS (M.J.B., D.W.S.) and the AMOS program, CSGB Division, OBES, DOE (M.J.B), and through the SLAC Laboratory Directed Research and Development Program (M.J.B., H.L.). Experiments were carried out at the LCLS at SLAC National Accelerator Laboratory operated by Stanford University on behalf of DOE, OBES. We thank K. Sauer for continuing scientific discussions. The atomic coordinates and structure factors have been deposited in the Protein Data Bank (www.pdb.org) with ID codes 4IXQ (dark state, S1) and 4IXR (first illuminated state, S2). See the supplementary materials for author contributions and full acknowledgments.

Supplementary Materials

www.sciencemag.org/cgi/content/full/science.1234273/DC1
Materials and Methods
Supplementary Text
Figs. S1 to S6
Tables S1 to S3
References (*31*–*41*)

19 December 2012; accepted 31 January 2013
Published online 14 February 2013;
10.1126/science.1234273

Insect Morphological Diversification Through the Modification of Wing Serial Homologs

Takahiro Ohde, Toshinobu Yaginuma, Teruyuki Niimi*

Fossil insects living some 300 million years ago show winglike pads on all thoracic and abdominal segments, which suggests their serial homology. It remains unclear whether winglike structures in nonwinged segments have been lost or modified through evolution. Here, we identified a ventral lateral part of the body wall on the first thoracic segment, the hypomeron, and pupal dorsolateral denticular outgrowths as wing serial homologs in the mealworm beetle *Tenebrio molitor*. Both domains transform into winglike structures under *Hox* RNA interference conditions. Gene expression and functional analyses revealed central roles for the key wing selector genes, *vestigial* and *scalloped*, in the hypomeron and the denticular outgrowth formation. We propose that modification, rather than loss, of dorsal appendages has provided an additional diversifying mechanism of insect body plan.

Insect ventral appendages, such as antennae, mouthparts, legs, and cerci, are serially homologous; they share anatomical and developmental features (*1*), despite morphological and functional differences along the body axis. The only known dorsal appendages in modern insects, however, are wings and their derivatives on the second and third thoracic segments. Winglike structures might have originally appeared on all thoracic and abdominal segments, and subsequently been repressed by *Hox* genes, which specify segment identities, in all but two thoracic segments (*2*). In the red flour beetle (*Tribolium castaneum*), RNA interference (RNAi) of the *Hox* gene *Sex combs reduced* (*Scr*) ortholog induced ectopic elytra formation in the prothorax (T1, the first thoracic segment) (*3*). Furthermore, ectopic pairs of wings formed in abdominal segments when the *Hox* genes *Ultrabithorax* (*Ubx*) and *abdominal-A* (*abd-A*) were repressed simultaneously (*3*). To explore putative wing serial homologs (WSHs), we examined the transformation from nonwing structure to wing by comparing weakly and strongly affected *Hox* RNAi phenotypes in the mealworm beetle (*Tenebrio molitor*), which is better suited to morphological analysis because it has a larger body than *T. castaneum*.

We initially isolated the *T. molitor Scr* homolog (*Tm-Scr*), and repressed its function by injecting double-stranded (ds) RNA into late-stage larvae (Fig. 1A). As in *T. castaneum,* ectopic elytra-like tissues formed on the first thoracic segment (T1) after *Tm-Scr* RNAi treatment (Fig. 1C), whereas dsRNA of the gene for enhanced green fluorescent protein (*egfp*) had no effect on adult phenotype (Fig. 1B). To identify the part that transformed into elytra-like tissue, we compared the phenotypes of *egfp* dsRNA–treated T1 with mildly and severely affected *Tm-Scr* RNAi T1. The *T. molitor* prothoracic tergum (pronotum) extends to the ventral side and forms the posterior collar of the procoxae (*4*). This ventral region of the pronotum is termed the hypomeron (Fig. 1E, left). The severe phenotype showed almost complete transformation (Fig. 1, H, K, and N versus Fig. 1, F, I, and L), whereas the mild phenotype showed incomplete transformation (Fig. 1, G, J, and M). The latter may represent an intermediate morphology between nonwing structure and wing. The mild phenotype showed cleft formation on the dorsolateral sides (arrowheads in Fig. 1, G and M), and morphological changes in the lateral body wall from the cleft to the ventral side, which corresponds with the hypomeron. The hypomeron elongated to form ectopic elytra-like structures in severely affected T1. From this observation, we conclude that *Tm-Scr* RNAi induced transformation from hypomeron into the wing, which suggests that the hypomeron is a WSH in the T1.

Larval RNAi of *T. molitor Ubx* and *abd-A* (*Tm-Ubx* and *Tm-abd-A*) resulted in the formation of six additional pairs of wings on the first to sixth abdominal segments (Fig. 1D). We could not determine whether the ectopic wing is mesothoracic elytra-like or metathoracic membranous wing–like, because vein formation is insufficient, and severely affected adults die before complete sclerotization. We investigated which abdominal structures transformed into ectopic wings when both *T. molitor Ubx* and *abd-A* homologs (*Tm-Ubx* + *abd-A*) were knocked down. *T. molitor* pupae have paired denticular outgrowths of the body wall on the dorsolateral side of the first to seventh abdominal segments (Fig. 1E, right, and R). The jaws on the anterior and posterior sides of the projecting flange are strongly sclerotized and toothed to form the gin-trap, a protective

Graduate School of Bioagricultural Sciences, Nagoya University, Chikusa, Nagoya 464-8601, Japan.

*Corresponding author. E-mail: niimi@agr.nagoya-u.ac.jp